Low Temperature Sintering of Fully Inorganic All-Solid-State Batteries – Impact of Interfaces on Full Cell Performance

Martin Ihrig[a,b], Martin Finsterbusch[a,c,d], Chih-Long Tsai[a], Alexander M. Laptev[a], Chia-hao Tu[e], Martin Bram[a], Yoo Jung Sohn[a], Ruijie Ye[a], Serkan Sevinc[a], Shih-kang Lin[e,f], Dina Fattakhova-Rohlfing[a,c,g], and Olivier Guillon[a,b,c,d]*

[a]Institute of Energy and Climate Research – Materials Synthesis and Processing, Forschungszentrum Jülich GmbH, 52425 Jülich, Germany

[b]Institute of Mineral Engineering, RWTH Aachen University, Mauerstr. 5, 52064 Aachen, Germany

[c]Jülich-Aachen Research Alliance: JARA-Energy, 52425 Jülich, Germany

[d]Helmholtz Institute Münster: Ionics in Energy Storage, Corrensstr. 46, 48149 Münster, Germany

[e]Hierarchical Green-Energy Materials Research Center National Cheng Kung University, No.1, University Road, Tainan City 701, Taiwan

[f]Department of Materials Science and Engineering, National Cheng Kung University, No.1, University Road, Tainan City 701, Taiwan

[g]Faculty of Engineering and Center for Nanointegration Duisburg-Essen, Universität Duisburg-Essen, Lotharstr. 1, 47057 Duisburg, Germany

*Corresponding author: Martin Finsterbusch:
E-mail: m.finsterbusch@fz-juelich.de Tel. +49 2461 61-2877 Fax: +49 2461 61-2455
Address: Forschungszentrum Jülich GmbH, Wilhelm Johnen Str., 52428 Jülich

Abstract

One of the necessary prerequisites to advance the electrochemical performance of $Li_7La_3Zr_2O_{12}$ (LLZ) based all-solid-state lithium batteries is the manufacturing of dense composite cathodes from cathode active material (CAM) and the LLZ ceramic solid electrolyte. However, free co-sintering of LLZ and CAM mixtures requires temperatures above 1000 °C which often leads to decomposition and secondary phase formation, especially for high energy CAMs. In our study we present a completely dry processing route which is fast, free of any sintering additives and coatings and suitable to fabricate dense mixed cathodes, pure LLZ separators and multilayers of the two. Through application of high mechanical pressure during Field-Assisted Sintering we were able to reduce the sintering temperature down to 675–750 °C with dwell times as low as 10 minutes, while still obtaining 95 % theoretical density for LCO/LLZ mixtures. The low sintering temperature is suitable for high energy CAMs, but leads to a significant effect of surface impurities, especially from powder handling in air, and affects the crystallinity of the CAM/LLZ interface. In the present paper we investigate the impact of resulting interfaces on the ionic conductivity, the interfacial impedance and the cycling stability of produced cells and propose the optimization strategy.

Keywords: all solid-state Li ion battery, composite cathode, garnet LLZ, high-pressure FAST/SPS, low temperature sintering, interface analysis

1. Introduction

Lithium secondary batteries (LIBs) are the systems of choice to power portable consumer electronics for entertainment, computing, telecommunication, and electric mobility as they offer high energy density, lightweight design and a longer lifetime than other battery types [1-4]. However, with the upscaling of LIBs, e.g. for application in electric vehicles, enhanced energy density and safety concern (due to use of flammable liquid electrolyte) has to be addressed in next

generation of batteries. In this regard, all-solid-state lithium ion batteries (ASSLB) on the basis of oxide ceramics attract attention of researchers and engineers due to their intrinsic safety, extended operational temperature and potential to achieve higher energy densities [1-3]. One of the most promising solid electrolytes is the garnet-type $Li_7La_3Zr_2O_{12}$ (LLZ) ceramic [5-7]. LLZ can crystallize in cubic or tetragonal phase. Both phases have a high lithium ion transference number ($t_{Li^+} \approx 1$) and good chemical stability versus metallic lithium. However, the ionic conductivity of tetragonal phase is two orders of magnitude lower than that of the cubic phase [7-13]. A partial substitution of Li and Zr in LLZ by Al or Ta stabilizes the LLZ in cubic phase at room temperature (RT) resulting in an excellent ionic conductivity of $>10^{-4}$ $S \cdot cm^{-1}$ [6]. Although LLZ can be handled in ambient air, prolonged exposure to air leads to the formation of an insulating layer of LiOH and Li_2CO_3 at the surface due to Li^+/H^+ exchange [14]. However, this insulating layer is usually removed during following heat treatment (e.g. sintering) with restoring of initial ionic conductivity [15].

Although the high ionic conductivity of LLZ make it very attractive as a solid electrolyte, the challenges during processing of LLZ and its integration in an electrochemical cell still hamper the development of LLZ-based ASSLBs. In particular, to achieve high energy density in such a cell, the cathode structure should provide high areal loading and full utilization of cathode active material (CAM), which requires efficient electronic and ionic conductive pathways. In an ideal cathode, CAM and electrolyte should form an intertwined 3D-network with a tight and well-developed contact between related phases. The interface between the CAM and the electrolyte should feature high total surface area with a low impedance to enable efficient charge transfer and transport with minimization of resistance losses in a battery. In a conventional Li ion battery, the extended cathode/electrolyte interface is formed spontaneously by infiltration of liquid electrolyte

in a porous CAM structures. As the infiltration cannot be realized for solid electrolytes (e.g. LLZ), other approaches to manufacture a dual phase cathode have to be explored. The easiest way for manufacturing of the dual phase cathode is sintering of a LLZ and CAM mixture.

However, LLZ typically requires a sintering temperatures of above 1050 °C with a dwell of a couple of hours to establish a good contact between individual grains and to achieve desired ionic conductivity. When LLZ is co-sintered with a CAM, the question of material stability during the processing is raised. Many mixtures of LLZ with CAMs such as $Li[Ni_{1-x-y}Co_xMn_y]O_2$ (NMC) or $Li_2NiMn_3O_8$ (LMO) show reduced thermodynamic stability [16]. Due to the oxidizing nature of CAMs, their reaction with LLZ occurs already at approximately 700 °C for NMC and at 500 °C for LMO, which is much lower than the thermal decomposition temperature of LLZ itself [17].

Some research groups have demonstrated that this thermodynamic limitation can be overcome or significantly lessened via a kinetic control of the sintering procedure, such as the reduction of sintering time, or the careful control of powder morphology and composition [18-21]. Several co-sintered composite cathodes show greatly increased CAM utilization and improved charge transport compared to pure CAM cathodes [22-26]. However, in spite of achieved progress, the formation during processing of secondary phases on CAM/solid electrolyte interface remains a serious limitation for cathode performance [16, 17, 27-29]. Furthermore, the relatively low density of composite cathodes prepared by conventional sintering via a slurry based route (around 80 %) leads to fracturing of weak sintered struts induced by volume change of CAM during electrochemical cycling [19].

As the interface reactions are kinetically controlled through thermal cycle, a faster processing with high heating and cooling rate, shorter dwell time and especially with lower sintering temperature might minimize the secondary phase formation. A decrease in sintering temperatures can be

achieved e.g. by using sintering additives or coating of CAM particles, for example by Nb- or Li_3BO_3 layers [28,30]. However, this layer alters the grain boundary composition and increases the interfacial resistance. For example, Li_3BO_3 has a Li ion conductivity of only 10^{-6} S cm^{-1} at room temperature (RT) which is much lower than that of LLZ (approximately 10^{-4} S cm^{-1} at RT) and can limit the charge transfer across the interface [31]. In order to avoid the use of sinter additives while still reducing sintering temperature and dwell time, an advanced sintering technique such as field assisted sintering, also known as spark plasma sintering (FAST/SPS) can be used [12]. By applying mechanical pressure and fast Joule heating, FAST/SPS enables sintering of dense ceramics at lower temperatures with significantly shorter dwell times as compared with conventional free sintering [12, 29, 32-38].

We previously reported the application of high-pressure FAST/SPS for the fabrication of $LiCoO_2$ (LCO) and LLZ composite cathodes, where a dense LCO/LLZ composite cathode was sintered at 675 °C with only 10 min dwell time [18]. The selected material pair was chosen based on its high chemical stability (over 1085 °C required, to observe side reactions between LCO and LLZ) and similar coefficients of thermal expansion. The LLZ was substituted with Ta and Al corresponding to the composition $Li_{6.45}Al_{0.05}La_3Zr_{1.6}Ta_{0.4}O_{12}$ (later denoted as LLZ:Ta) to maintain the cubic stricture and to increase the ionic conductivity [39].

Following this work, we now demonstrate that FAST/SPS enables the fabrication of different components of ASSLB without sintering aids, such as a dense LLZ:Ta separator layer with high ionic conductivity, a dense LCO/LLZ:Ta composite cathode and an integrated cathode half-cell consisting of a composite cathode and a LLZ:Ta separator layer at temperatures as low as 675 ° - 750 °C. Analyzing structure, morphology and electrochemical performance of the obtained components, we found that the grain boundary crystallinity and the impurities appearing on

particles surface (i.e. LiOH or Li_2CO_3) play a decisive role in the formation of highly conductive interfaces and in the minimization of porosity within the fabricated components. The removal of these impurities prior FAST/SPS processing ensures high ionic conductivity even at low sintering temperature and improved mechanical and cycling stability of composite cathodes in ASSLBs.

2. Experimental

2.1. Powder preparation

Ta- and Al-substituted LLZ powder ($Li_{6.45}Al_{0.05}La_3Zr_{1.6}Ta_{0.4}O_{12}$, LLZ:Ta) was synthesized by solid-state reaction as reported previously [19]. The calcined LLZ:Ta cake was ground in a mechanical mortar RM200 (Retsch). The resulting particles had a spongy shape with a particle size of D_{10} = 5.8 µm, D_{50} = 10.0 µm and D_{90} = 16.4 µm as determined by the laser light scattering method in a LA950 device (Retsch). This powder will be denoted below as LLZ-air powder. Some amount of LLZ:Ta powder was additionally processed to test the impact of surface contamination from air on electrochemical performance. A part of the LLZ:Ta powder was pressed into loose pellets to prevent Li loss and Al diffusion from the Al_2O_3 crucible and annealed in Ar at 750 °C for 2 h to remove surface impurities (LiOH and Li_2CO_3). The sintered cake was crushed into powder in an Ar-filled glovebox. The obtained powder consisted of particles with nearly the same shape and size as the non-annealed powder with D_{10} = 6.6 µm, D_{50} = 12.2 µm and D_{90} = 22.5 µm (Supporting Information, Fig. S1). This powder will be named later as LLZ-annealed.

For fabrication of composite cathodes, a portion of Ar-treated or untreated powder was mixed with $LiCoO_2$ (LCO) CAM powder (Alfa Aesar, 99.5 %) in a 1:1 wt. ratio on a rolling bench RW20 (IKA) at 200 rpm for 100 h in air when using the LLZ-air powder or in Ar atmosphere for the LLZ-annealed powder. The Ar-annealed LLZ:Ta powder and its mixture with LCO were stored in an Ar-filled glovebox (<0.1 ppm H_2O and O_2) all the time before following sintering.

2.2. Pellet sintering

The pellets with one or two layers (for the use as a half-cell) were manufactured by FAST/SPS sintering. In one case, LLZ-air, LLZ-annealed powder or their mixture with LCO was used. In another case, the first layer consisted of LLZ and LCO mixture and the second layer was comprised of pure LLZ-air or LLZ-annealed powder. A schematic overview of the prepared pellets is shown in Fig. 1.

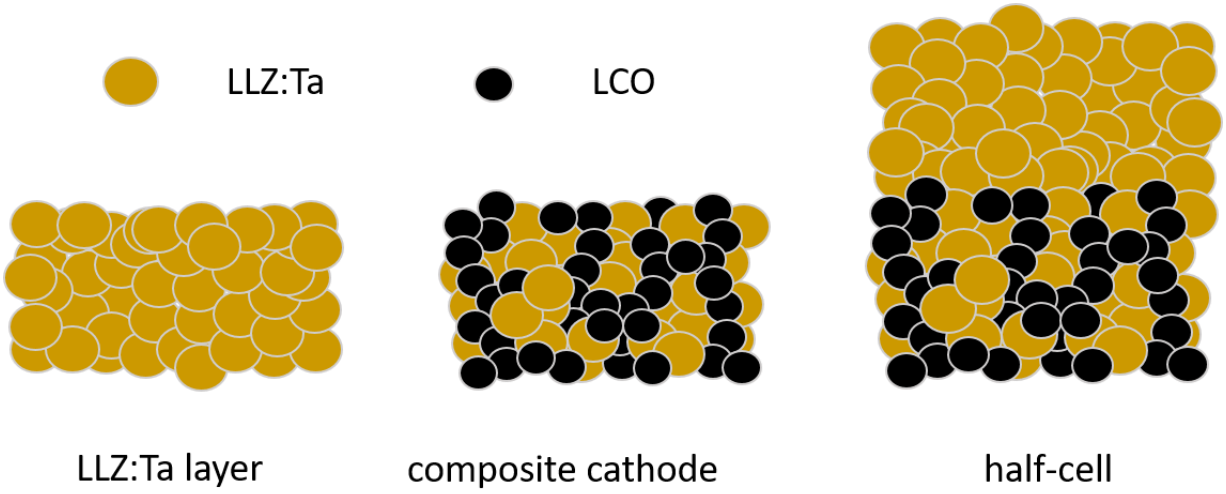

Fig. 1. Schematic overview of manufactured battery components.

For manufacturing of pellets with a single layer, a portion of 0.5 g of LLZ-air, LLZ-annealed powder or their mixture with LCO was poured into a metallic mould made of molybdenum based alloy TZM (Plansee SE). The mould had an inner diameter of 12 mm that was covered by wound graphite foil (SGL Carbon). The TZM punches were also separated from powder by two discs punched from graphite foil to prevent their sticking with sintered pellet.

For the half-cell, 0.5 g of powder mixture was firstly poured in the mould and pressed at 50 MPa, followed by adding another 1 g of LLZ:Ta powder and pressing with the same pressure again.

The powders and powder mixtures were sintered in a HP D 5 FAST/SPS device (FCT Systeme). The sintering was performed at a temperature of 675 °C, 750 °C or 800 °C with 10 min dwell time in Ar flow. The heating rate was 100 K min^{-1} and the cooling was 20 K min^{-1}. A sintering temperature of 675°C is slightly below an onset temperature of 700°C for reaction between LCO and graphite foil as explained in detail in our previous paper [18]. A temperature of 750°C is somewhat higher than the above-mentioned onset temperature. However, the reaction between LCO and graphite at this temperature is still not pronounced [18]. The sintering at 800 °C was performed to verify the phase stability at higher temperature. A mechanical pressure of 50 MPa or 440 MPa was applied before the heating in all experiment. The loading with 50 MPa is typical for FAST/SPS sintering in a standard graphite mould [32]. A pressure of 440 MPa is the highest pressure which can be achieved in a 12 mm mould under a maximal load of 50 kN for HP D 5 device. After FAST/SPS sintering the graphite foil was polished off from all pellet's surfaces by SiC sandpaper.

2.3. Cell fabrication

The half-cells, consisting of a composite cathode and an LLZ:Ta separator, were either directly polished with SiC sandpaper to erase any possible surface impurities or annealed at 1050 °C in air for 30 minutes before battery assembling. The half-cells were sputter coated with Au for 30 s to support the adhesion of an In anode on the LLZ:Ta side and for 150 s on the cathode side to serve as current collector (Cressingtion 108 sputter coater). Afterwards, the half-cells were transferred into an Ar-filled glovebox (<0.1 ppm H_2O and O_2). On the LLZ:Ta-side, a metallic In foil was mechanically pressed on the samples to act as anode. The assembled ASSLBs were placed into Swagelok cells and sealed before taking from the glovebox. The amount of active material in the composite cathodes was estimated by measuring of thickness and diameter of the cathode and by

using of average density of the LCO/LLZ:Ta mixture. The composite cathode with LLZ-air and LLZ-annealed for the ASSLBs had both a thickness of roughly 55 µm and a CAM loading of 16 mg.

2.4. Microstructural and density characterization

The phase analysis was performed by X-ray diffraction method (XRD) using a D4 Endeavor (Bruker) device and Bragg-Brentano configuration in the 2θ range from 10° to 80° with a step of 0.02° and with Cu K-alpha radiation. The XRD device was equipped with a LYNXEYE energy-dispersive 1D detector (Bruker). The HighScore software (Malvern Panalytical) with PDF-2 database (ICDD) was used for qualitative phase analysis. The Rietveld analysis for quantification of results was conducted using the TOPAS 4.2 software (Bruker).

The density of pellets was determined from their geometry and mass. The density for LCO/LLZ:Ta pellets was calculated by using a theoretical density of 5.2 g cm^{-3} as an average from LLZ:Ta (5.3 g cm^{-3}) and LCO (5.1 g cm^{-3}) densities [40].

The microstructure of pellets was investigated by a scanning electron microscope (SEM) TM3000 (Hitachi). The samples for transmission electron microscopy (TEM) were cut out of a polished cross section by a dual beam-focused ion beam with 30 keV and 10 pA within a Helios NanoLab G3 CX device (FEI) and transferred to carbon lacy TEM grid by a glass tip micro-manipulator. The TEM images were recorded with a JEM-2100F electron microscope (JEOL) operated at 200 kV.

2.5. Electrochemical characterization

The electrochemical experiments were performed at either 25 °C or 80 °C within a climate chamber VT 4002EMC (Vötsch Industrietechnik) using a VMP-300 multichannel Potentiostat

(BioLogic). The electrochemical impedance spectroscopy (EIS) was performed in VMP-300 multichannel Potentiostat in the frequency range from 3 MHz to 10 mHz and with an amplitude of 10 mV for perturbation field. The fits for the impedance spectra were performed using ZView software (Scribner). Long term galvanostatic cycling was done with constant-current-constant-voltage (CC-CV) mode for charging and with constant current for discharging. The batteries were charged to 3.4 V vs In-Li (i.e. 4.0 V vs. Li/Li^+) with a constant current density of 50 μA cm^{-2} and held at this voltage to allow the current density to drop to 10 μA cm^{-2}. Discharge of the batteries was done with a constant current density of 50 μA cm^{-2} until the voltage was dropped to 2.8 V vs Li-In.

3. Results and discussion

The composite cathodes produced by FAST/SPS technique were first analyzed with respect to the phase stability under process conditions. To assess the impact of surface contamination in air, pure LLZ:Ta powder stored and treated in air (LLZ-air) and LLZ:Ta powder annealed in Ar (LLZ-annealed) were used to fabricate the single layer separators. The obtained samples were characterized with respects to microstructure and electrochemical properties. Finally, the full cells consisting of mixed LCO/LLZ cathode and LLZ separator, produced with optimized parameters, and with In anode were electrochemically tested.

3.1. Phase stability of composite cathode

The phase stability of LCO and LLZ:Ta is essential to achieve good interfacial and bulk ion and electron transport in LCO/LLZ composite cathode. The phase stability of a LCO/LLZ-air composite cathode was investigated by comparing of corresponding XRD patterns with XRD patterns of pristine LCO and LLZ-air powders (Fig. 2). All observed peaks are sharp and indicate the good crystallinity after FAST/SPS sintering. The composite cathodes prepared at a relatively

low applied pressure of 50 MPa, show, besides the typical peaks for rhombohedral LCO and cubic LLZ:Ta, some other peaks with low intensities at both sintering temperatures i.e. 675 °C and to 800 °C (Fig. 2a). Rietveld refinement suggests that these peaks are related to $La_2Li_{1-x}Co_xO_4$ (23°, 27° and 32°) and CoO (36°, 42° and 61 °) with an amount of 10 wt. % and 11 wt. % for the samples sintered at 675 °C and 800 °C, respectively. (Supporting Information, Table S1).

At a high FAST/SPS pressure of 440 MPa the XRD patterns show the high crystallinity as well (Fig. 2b). However, the intensity of peaks related to side phases is drastically reduced. The Rietveld analysis gives only 4 wt. % of side phases for 675°C and 750°C sintering temperature. For 800 °C the side phase content increases up to 13 wt. %, again showing $La_2Li_{1-x}Co_xO_4$, CoO and additionally $La_2Zr_2O_7$ (34°) phases.

The striking difference in secondary phase formation between FAST/SPS sintering at 50 MPa and 440 MPa can be understood when considering the effect of applied pressure and short sintering time on the origin of the secondary phases. First, the appearance of CoO is a direct result of reaction between LCO and graphite foil at temperatures above 500 °C resulting in formation of Li_2O, CO_x, and CoO [18, 41,42]. Once the pressure-assisted sintering starts, the pores and thus the free surface area available for reaction is quickly reduced limiting carbon diffusion into the sample. Only the material in direct contact with graphite foil decomposes but can later be removed by surface polishing. From this point of view, the application of pressure before heating is beneficial for reduction of LCO decomposition during heating process (Supporting Information, Fig. S2).

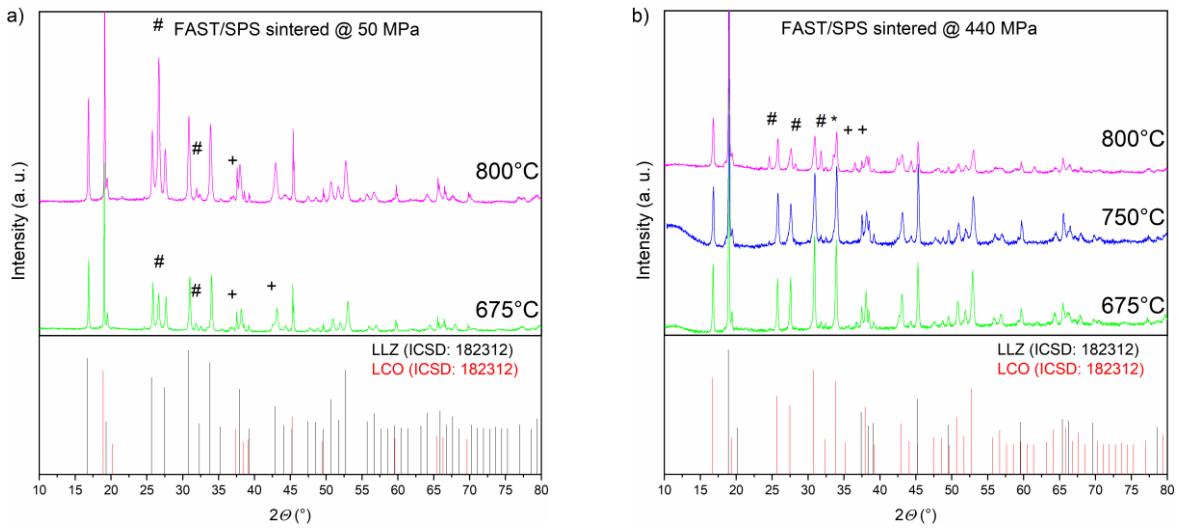

Fig. 2. XRD patterns of pristine LCO and LLZ-air powders and sintered LCO/LLZ-air composite cathode. The composite cathode was sintered by FAST/SPS at different temperatures under a pressure of: a) 50 MPa and b) 440 MPa. The side phases are marked with: # for $La_2Li_{1-x}Co_xO_4$, + for CoO, and * for $La_2Zr_2O_7$.

Second, the products of reaction between LCO and LLZ:Ta, such as $LaCoO_3$, La_2CoO_4 or Co-substituted LLZ:Ta, are often formed in conventionally sintered LCO/LLZ samples due to long sintering time [17,43]. Short heating and dwell time in FAST/SPS process kinetically limit these reactions, contributing to the reduced amounts of secondary phases. Moreover, the reactions are further limited by low sintering temperatures used during FAST/SPS, which are far below the reported 1085 °C at which LCO and LLZ start to react with a visible rate [44].

Third, the formation of a pyrochlore $La_2Zr_2O_7$ phase due to delithiation of LLZ is also often observed in conventionally sintered samples [15, 45-47]. In FAST/SPS process, short sintering time, applied pressure and closed sintering mould, result in negligible Li loss due to evaporation or reaction with carbon from the graphite foil up to 750°C (Fig. 2).

3.2. Influence of LLZ:Ta pretreatment

To investigate the impact of surface contaminants from air, we first studied a single LLZ:Ta separators prepared by FAST/SPS with respect to achieved density, microstructure and electrochemical properties. Several research groups reported formation of $Li_{7-x}H_xLa_3Zr_2O_{12}$ and LiOH when LLZ was exposed to moisture from air according to reaction (1). Subsequently, LiOH converts to Li_2CO_3 due to interaction with CO_2 [48-51]. Besides, CO_2 might also directly react with LLZ (reaction 2) [14].

$$Li_7La_3Zr_2O_{12} + xH_2O \rightarrow Li_{7-x}H_xLa_3Zr_2O_{12} + xLiOH \quad (1)$$

$$Li_7La_3Zr_2O_{12} + xCO_2 \rightarrow Li_{7-2x}La_3Zr_2O_{12-x} + xLi_2CO_3 \quad (2)$$

With using of Raman spectroscopy, we also observed the formation of Li_2CO_3 layer on LLZ:Ta surface within a few hours of air exposure (Supporting Information, Fig. S3). According to the literature, the Li_2CO_3 can form a closed layer of around 30 nm in thickness on LLZ particles within a few days of exposure to air [23]. Larraz et al. notice that the reactions described by equations (1) and (2) are reversible at temperatures above 400 - 450 °C and 650 C°- 700 °C, respectively [15]. Besides both materials, LiOH and Li_2CO_3, melt and start to decompose at either 450 °C or 720 °C. In our case, this means that the sintering temperature of 750 °C during our FAST/SPS process is sufficiently high to remove LiOH, but the Li_2CO_3-layer might not be removed at this sintering temperature, since the dwell time of only 10 min is rather short compared to the commonly used 2 h annealing in Ar at 750 °C [52].

In order to investigate the impact of LiOH and Li_2CO_3 surface impurities on the sintering behavior and the electrochemical properties, two types of LLZ:Ta powders were used for the fabrication of LLZ:Ta separators and composite cathodes. In the first set of experiments, LLZ:Ta powder stored in air for a couple of days was used for sample preparation (LLZ-air). In the second set of

experiments, a part of this powder was annealed in Ar at 750 °C for 2 h (LLZ-annealed) before using. It is worth to mention that the particle size of the LLZ:Ta did not significantly change by this treatment (see Section 2.1 for more detail).

3.3. Density and microstructure

High storage capacity of ASSLB requires a high density of sintered components. The application of high-pressure FAST/SPS (a pressure of 440 MPa) for sintering components with LLZ-air or LLZ-annealed powder results in high densities of single LLZ layers and composite cathodes (Table 1). An exceptional feature of developed high-pressure FAST/SPS process is the possibility to achieve a relative density of over 90 % at sintering temperatures as low as 675 °C without the use of any sintering aids. As expected, the relative density slightly increases for a higher sintering temperature of 750 °C to 92 % and 95 % for the pure LLZ:Ta and for the composite cathode, respectively. The relative density of LLZ:Ta and the composite cathode seems not to be affected by the way of powder preconditioning within the error of density measurements (around ±1 %).

Table 1. Relative density (%) of pure LLZ:Ta layer and LCO/LLZ composite cathode sintered by FAST/SPS at 440 MPa in Ar with a dwell time of 10 min at two temperatures.

FAST/SPS temperature	Pure LLZ:Ta layers		Composite cathodes	
	LLZ-air	LLZ-annealed	LLZ-air	LLZ-annealed
675°C	90%	90%	92%	92%
750 °C	92%	92%	95%	95%

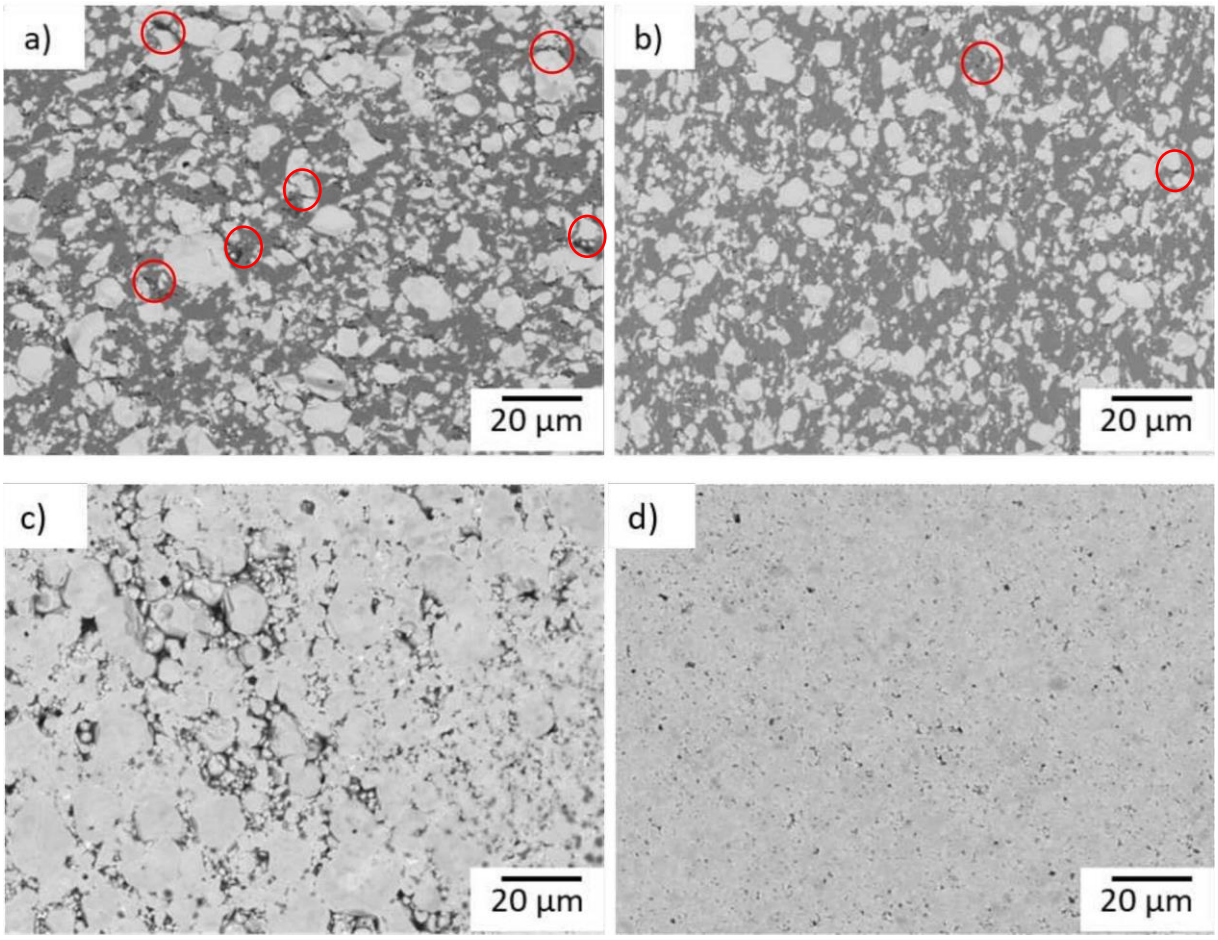

Fig. 3. Cross-sectional SEM images of LLZ:Ta/LCO composite cathodes (a, b) and pure LLZ:Ta layers (c, d) after FAST/SPS at 750 °C and 440 MPa in Ar with 10 min dwell time. a) The composite cathode prepared with LLZ-air powder. b) The composite cathode prepared with LLZ-annealed powder. The areas in bright are LLZ:Ta and dark are LCO, black areas represent pores (some of them are marked with red circles). c) The LLZ:Ta monolayer prepared with LLZ-air powder. d) The LLZ:Ta monolayer prepared with LLZ-annealed powder.

The cross-sectional SEM images of composite cathodes prepared with LLZ-air and LLZ-annealed powders are shown in Fig. 3a and Fig. 3b. The LCO and LLZ:Ta grains can be clearly distinguished. The LCO and LLZ:Ta phases are homogenously distributed throughout the whole volume, which is beneficial for their application in ASSLBs. Even if the average densities of both

composite cathodes are similar (92 %), the local microporosity is somewhat different for the LLZ:Ta powders treated in different ways. The composite cathode prepared with LLZ-air powder has a larger number of micropores predominantly on boundaries of LLZ-air grains. The composite cathode prepared with LLZ-annealed has a lower number of micropores. This difference can be attributed to the removal of LiOH (melting and decomposition at 450°C) and Li_2CO_3 (melting and decomposition at 720°C) during FAST/SPS sintering at 750 °C. The same observation is true for pure LLZ:Ta separators. The LLZ-air and LLZ-annealed pellets sintered at 750 °C (Fig. 3c and Fig.3d) have distinctly different microstructures. The separator prepared from the LLZ-air powder, although being compact, features rather a large amount of small encapsulated micropores and a few relatively large pores evenly distributed through the sintered body. The smaller micropores are formed predominantly around LLZ grains. These pores lead to structural weak points within the LLZ-air separator and cause break outs during polishing of the surface. Due to the same relative density of LLZ-air and LLZ-annealed (in the framework of measurement accuracy), we assume that the break outs explain the large pores. In contrast, the pellet obtained from LLZ-annealed powder shows fewer small encapsulated micropores and no larger ones, preventing break outs during sample polishing.

3.4. Impact of surface impurities on electrochemical performance

In order to show that the pores in the microstructure of composite cathodes and separators are a result of LiOH and Li_2CO_3 removal, EIS measurements on pure LLZ-air and LLZ-annealed separator were performed (Fig. 4). Both LLZ-air and LLZ-annealed separator sintered at 750 °C (Fig. 4a and Fig.4b) are comparable with each other and show one semicircle at high frequencies, another one at medium frequencies and the tail from the Au blocking layer. The EIS data were fitted with an equivalent circuit shown in Fig. 4 where R represents an ohmic resistance and CPE

is a constant phase element. The semicircle at high frequencies (MHz range) is commonly attributed to the bulk resistance [48]. The semicircle at mid frequencies (kHz range) correspondingly represents the grain boundary resistance. The fitting values can be found in Supporting Information, Table S2.

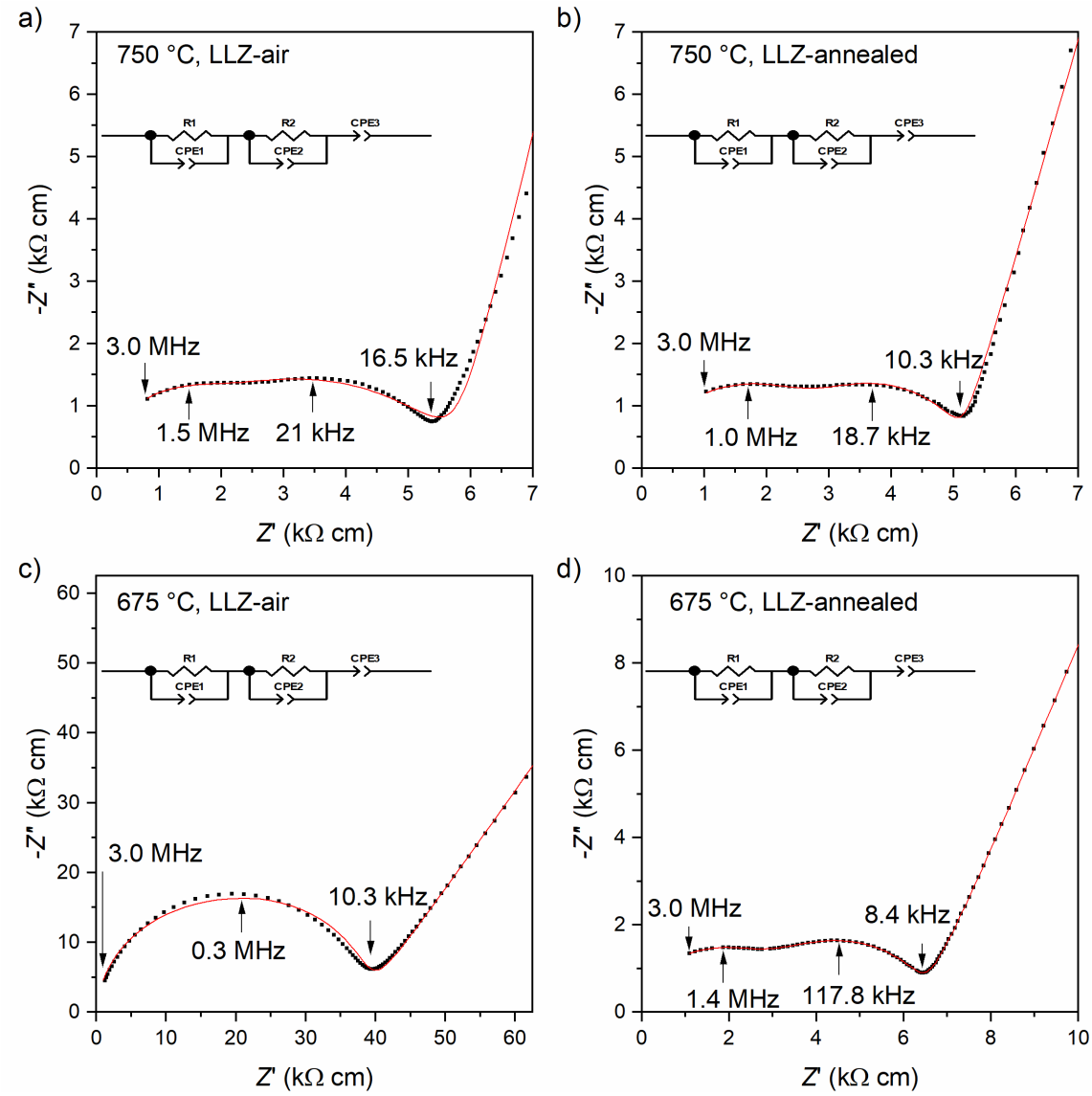

Figure 4. Nyquist-plot for LLZ-air and LLZ-annealed pellets sintered by FAST/SPS at 675°C and 750°C with 10 min dwell in Ar and under a pressure of 440 MPa. Fitting (red lines) was performed

with related equivalent circuit. The full EIS spectra can be found in Supporting Information, Fig. S4.

The LLZ-air and LLZ-annealed separators sintered at 750°C have comparable bulk impedance with 3002 Ω cm and 2642 Ω cm respectively. Thus, the pretreatment does not alter the grain conductivity significantly. The grain boundary resistance for the LLZ-air sample is 2407 Ω cm and is similar to that for LLZ-annealed with 2529 Ω cm. The resulting total conductivity is around 2×10^{-4} S cm^{-1} for both types of LLZ:Ta. The rather similar grain boundary resistance proves the removal of LiOH and Li_2CO_3 layers during FAST/SPS sintering at 750°C. In contrast, the LLZ-air and LLZ-annealed pellets sintered at 675 °C show a completely different behavior (Fig. 4c and Fig. 4d). While the LLZ-annealed pellet shows a similar total ionic conductivity of around 1×10^{-4} S cm^{-1} (6.9 kΩ cm), the LLZ-air pellet exhibits only 3×10^{-5} S cm^{-1} (39 kΩ cm). For LLZ-air sintered at 675 °C, it is also not possible to separate the bulk from the grain boundary contribution (Fig. 4c and Supporting Information, Table S2). However, if we assume that the bulk impedance is similar as was shown for LLZ-air and LLZ-annealed sintered at 750 °C, the reduction in total ionic conductivity must be caused by the remaining LiOH and Li_2CO_3 layer on the LLZ-air grains. Although the removal of LiOH and Li_2CO_3 during sintering at 750°C leads to similar total ionic conductivities as for pretreated samples, the observed formation of pores can result in structural weak points (Fig. 3). These might cause the mechanical fracturing and lead to capacity fading due to volume change of LCO during de-/lithiation.

3.5. Investigation of LCO/LLZ-annealed interface

For a detailed study of the LCO/LLZ-annealed interface, the TEM investigation of a composite cathode was performed. The obtained results are shown in Fig. 5. The TEM image of the as-

prepared composite cathode (Fig. 5a) shows the crystalline grains of LCO and LLZ-annealed. This agrees well with the XRD results (Fig. 2). However, between the LCO and LLZ-annealed grains an amorphous layer with a thickness of roughly 5 nm was formed. Amorphous interfaces are known to be detrimental for conduction processes [53,54]. For example, in cold sintered solid electrolytes, amorphous interfaces are typically observed and are considered to be a reason for low total ionic conductivity. In particular, Leng et al. observed a low total ionic conductivity for cold sintered $Na_3Zr_2Si_2PO_{12}$. By applying a subsequent annealing step the total ionic conductivity increased by an order of magnitude. The increase in ionic conductivity was explained by crystallization of amorphous grain boundary layer [54].

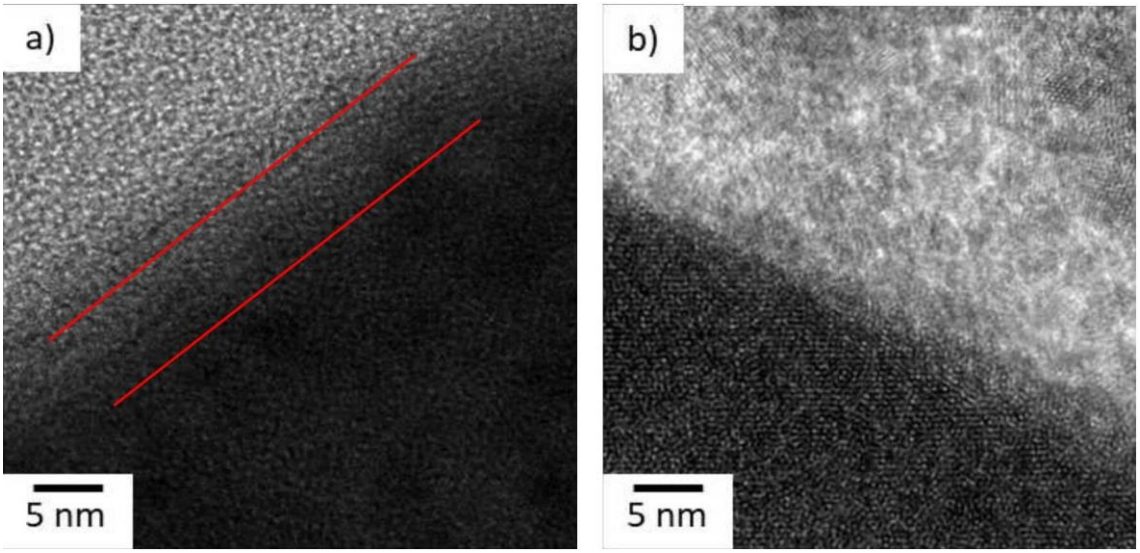

Fig. 5. TEM images of the interface between LCO (bright area) and LLZ:Ta (dark area): a) as prepared composite cathode; b) post-annealed composite cathode. The interface between LCO and LLZ:Ta in the as-prepared composite cathode appears amorphous (marked by red lines). Post-annealing resulted in crystallization of amorphous interface.

In order to verify this hypothesis, a post-annealing step at 1050°C, 30 min in air was introduced for our samples. This additional heat treatment leads to crystallization of the LCO/LLZ-annealed

interface (Fig. 5b) without causing side reactions (Supporting Information, Fig. S5). The LCO and LLZ-annealed phases are clearly distinguishable in Fig. 5b and are in sharper appearance than that for the as-prepared interface in Fig. 5a. Only small isolated amorphous areas can be found between LCO and LLZ-annealed grains. To evaluate the effect of the post-annealing on total cell resistance, two half-cells were prepared with LLZ-annealed powder. One of them was post-annealed at 1050°C before assembling them into an ASSLB. Both ASSLBs (as-prepared and post-annealed) were charged to 3.4 V vs In-Li (4 V vs Li/Li^+) and EIS was performed (Fig. 6).

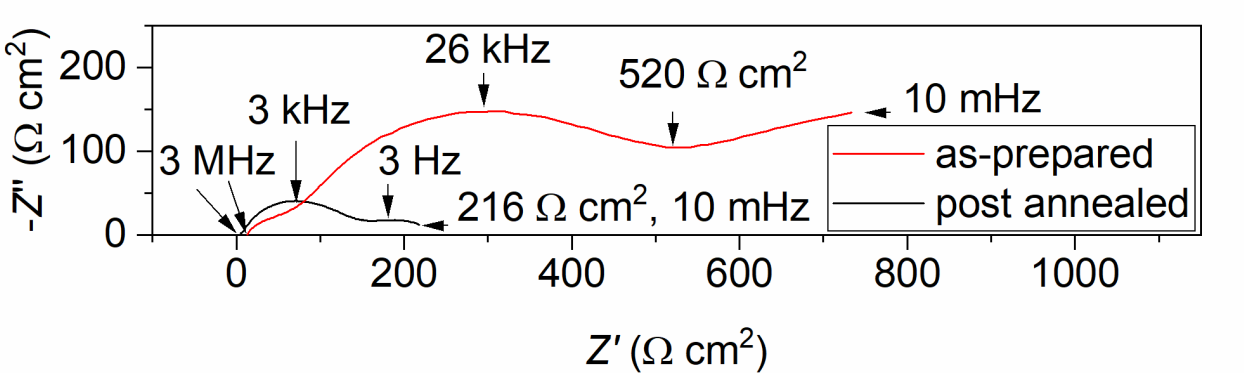

Fig. 6. EIS spectra of ASSLBs consisting of LCO/LLZ:Ta|LLZ:Ta|In-Li at 80 °C. The ASSLBs were charged to 3.4 V vs In-Li at 50 µA cm^{-2} beforehand. The composite cathode was either used as-prepared (red line) or with post-annealing at 1050 °C for 30 min in air (black line).

For the as-prepared ASSLB two depressed semicircles can be observed. In the post-annealed ASSLB, two smaller semicircles were observed. While for the as-prepared sample the high frequency semicircle is smaller, this was switched after post-annealing. This can be a result of different overlap of grain, grain boundary, and interfaces between cathode/LLZ-air and anode/LLZ-annealed.

The total impedance of the ASSLB was estimated from the end of second semicircle. The as-prepared ASSLB has an areal resistance of 520 Ω cm^2. For the post-annealed ASSLB this value is

only 216 Ω cm^2. Thus, the total cell resistance of ASSLB can be reduced by a post-annealing step. The microstructure of the composite cathode was unaltered after post-annealing (Supporting Information, Fig. S6). Therefore, the reducing of total cell resistance is apparently a result of higher crystallinity of boundary between LCO and LLZ-annealed grains.

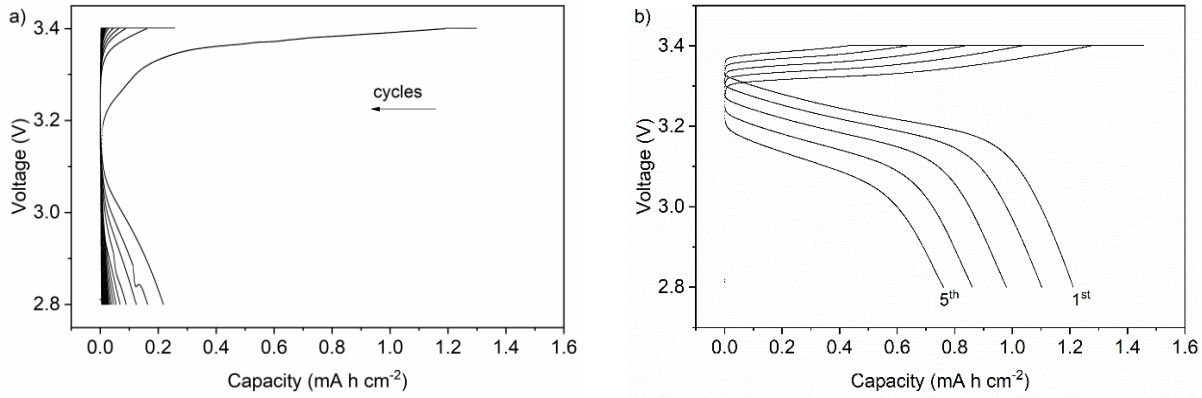

Fig. 7. Charge-discharge characteristics of ASSLB (LCO/LLZ:Ta|LLZ:Ta|In-Li) at 80 °C after post-treatment at 1050 °C and with a charge and discharge current density of 50 µA cm^{-2}. a) LLZ:Ta powder stored in air (LLZ-air) containing surface impurities was used. b) The impurities where removed by annealing in Ar (LLZ-annealed).

3.6. Electrochemical performance of full cells

Finally, the impact of LLZ surface impurities on electrochemical performance of ASSLB cell was tested. Two cells were manufactured as describe in Section 2.3 using LLZ-air or LLZ–annealed powder. Both ASSLB cells were post-annealed. The charge/discharge behavior of the ASSLBs is shown in Fig. 7. The ASSLB were charged only to 3.4 V (4.0 V vs Li/Li^+) to minimize the volume change of LCO during cycling for limiting the risk of mechanical degradation [55, 56]. The first charge is comparable for both ASSLBs and shows the typical behavior of LCO. The LCO utilization of the first charge is for the ASSLB with LLZ-air is 81 mAh g^{-1} or 1.3 mAh cm^{-2} and

LLZ-annealed is 94 mAh g^{-1} or 1.5 mAh cm^{-2}. The high areal capacities show that the composite cathodes, in comparison to pure LCO cathodes, show much higher LCO utilization [26].

However, the discharge greatly varies between LLZ-air and LLZ–annealed. For the ASSLB prepared with LLZ-air, the first discharge does not resemble the typical LCO behavior and has a much lower capacity of 0.2 mAh cm^{-2} as compared to the LLZ-annealed ASSLB of 1.2 mAh cm^{-2}. This can be explained by the LCO utilization of 14 mAh g^{-1} for the LLZ-air ASSLB and 75 mAh g^{-1} for the LLZ-annealed ASSLB. The low coulombic efficiency points to a strong degradation of the electrode already in the first charge/discharge cycle. The low coulombic efficiency might be due to high polarization and high total resistance of the composite cathode. The high impedance can originate from: (i) unfavourable chemical composition of the interfaces due to the presence of surface impurities; (ii) not complete sintering of the LCO and LLZ:Ta powders e.g. due to presence of surface impurities; (iii) presence of micropores and microcracks between the LCO and LLZ:Ta phases caused by decomposition of surface impurities. The latter effect can be also responsible for the possible lower mechanical stability of mixed cathodes that can mechanically degrade due to the volume change during charging. Therefore, the ASSLB has high charge capacity but due to damaged interface most of the LCO might not be adequate discharged. For the ASSLB prepared using LLZ-annealed, the curves maintain the typical LCO behavior over multiple cycles. However, the hysteresis between the potential plateaus for charge and discharge gradually increases in each subsequent cycle.

As the LLZ:Ta pretreatment is different while the ASSLBs are otherwise same, it is reasonable to expect that the surface impurities must be responsible for the faster capacity fading in the ASSLB with LLZ-air. Earlier, the formation of pores around LLZ:Ta grains due to the removal of LiOH and Li_2CO_3 layers for LLZ-air was observed (Fig. 3a). These pores reduce the mechanical stability,

making the microstructure prone to crack propagation during cycling, caused by approx. 4 % volume change of LCO [55]. Therefore, capacity fading caused by mechanical fracturing, as discussed by Tsai et al. for a similar ASSLB is most likely [19]. For the ASSLB fabricated with LLZ-annealed the crack formation should be slower due to lower number of micropores (see Fig. 3). In conclusion, it is important to control the surface purity of initial powders LLZ:Ta as it has a strong effect on electrochemical performance and cycling stability of ASSLBs.

4. Conclusion

Fully inorganic ASSLBs featuring a composite LCO/LLZ cathode and LLZ separator were prepared by FAST/SPS technique without the use of sintering aids. They showed high areal discharge capacities of up to 1.2 mAh cm^{-2} but only low cycling stability.

In contrast to conventional sintering of LCO/LLZ mixed cathodes at around 1050 °C, the sintering temperature was reduced to 750 °C and even to 675 °C with application of a high mechanical pressure. Thereby, a relative density of at least 90 % and a reasonable ionic conductivity at RT were achieved. This sintering approach opens the opportunity to use other active materials such as NMC or NCA that exhibit a severe decomposition above 700 °C or 500 °C. A further study to evaluate the possibility of co-sintering of these materials by high-pressure FAST/SPS has to be conducted.

It was also shown, that the pretreatment of LLZ:Ta at 750°C is crucial for subsequent low temperature sintering at around or below the decomposition temperature of Li_2CO_3, which is present on the surface of LLZ powder stored in air. The detrimental effect of residual impurities on interface conductivity and mechanical properties leads to reduced electrochemical performance in ASSLB components and cells, especially to low cycling stability. Furthermore, a free of impurity LCO/LLZ:Ta interface was investigated, and amorphous layers were identified

negatively impacting the full cell performance. This layer can be crystallized by post-annealing at 1050°C with significant improvement of electrochemical performance. However, the development of new strategies to avoid the amorphization of LCO/LLZ interface is needed in order to fully capitalize the advantages of high-pressure FAST/SPS at manufacturing of ASSLBs.

Supporting Information

Supplementary data related to this article can be found at …

Acknowledgment

Financial support by the German Federal Ministry of Education and Research (Federal ministry of education and research) is gratefully acknowledged. The authors would like to thank Grit Häuschen for synthesizing the LLZ:Ta powder, Andrea Hilgers for measurement of particle size distribution and Mark Kappertz for preparation of cross sections for SEM.

Funding

This work was supported by the German Federal Ministry of Education and Research (Bundesministerium für Bildung und Forschung) [project # 13XP0134A (EvaBatt)]

References

[1] Y. Xiao, Y. Wang, S.H. Bo, J.C. Kim, L.J. Miara, G. Ceder, Understanding interface stability in solid-state batteries. Nat Rev Mater 5 (2019) 105-126. https://doi.org/10.1038/s41578-019-0157-5
[2] J. Janek, W.G. Zeier, A solid future for battery development. Nat Energy 1 (2016) 16141. https://doi.org/10.1038/nenergy.2016.141
[3] Y. Ren, K. Chen, R. Chen, T. Liu, Y. Zhang, C.W. Nan, Oxide electrolytes for lithium batteries. J Am Ceram Soc 98 (2015) 3603-3623. https://doi.org/10.1111/jace.13844
[4] J. M. Tarascon, M. Armand, Issues and challenges facing rechargeable lithium batteries. Nature 414 (2001) 359-367. https://doi.org/10.1038/35104644
[5] M. Rawlence, I. Garbayo, S. Buecheler, J.L.M. Rupp, On the chemical stability of post-lithiated garnet Al-stabilized $Li_7La_3Zr_2O_{12}$ solid state electrolyte thin films. Nanoscale 8 (2016) 14746-14753. https://doi.org/10.1039/C6NR04162K
[6] V. Thangadurai, S. Narayanan, D. Pinzaru, Garnet-type solid-state fast Li ion conductors for Li batteries: critical review. Chem Soc Rev 43 (2014) 4714-4727. https://doi.org/10.1039/C4CS00020J

[7] C. Wang, K. Fu, S.P. Kammampata, D.W. McOwen, A.J. Samson, L. Zhang, G.T. Hitz, A.M. Nolan, E.D. Wachsman, Y. Mo, V. Thangadurai, L. Hu, Garnet-type solid-state electrolytes: materials, interfaces, and batteries. Chem Rev 120 (2020) 4257-4300. https://doi.org/10.1021/acs.chemrev.9b00427
[8] V. Thangadurai, D. Pinzaru, S. Narayanan, A.K. Baral, Fast solid-state Li ion conducting garnet-type structure metal oxides for energy storage. J Phys Chem Lett 6 (2015) 292-299. https://doi.org/10.1021/jz501828v
[9] Y. Ren, H. Deng, R. Chen, Y. Shen, Y. Lin, C.W. Nan, Effects of Li source on microstructure and ionic conductivity of Al-contained $Li_{6.75}La_3Zr_{1.75}Ta_{0.25}O_{12}$ ceramics. Journal Eur Ceram Soc 35 (2015) 561-572. https://doi.org/10.1016/j.jeurceramsoc.2014.09.007
[10] Y. Zhu, X. He, Y. Mo, First principles study on electrochemical and chemical stability of solid electrolyte–electrode interfaces in all-solid-state Li-ion batteries. J Mater Chem A 4 (2016) 3253-3266. https://doi.org/10.1039/C5TA08574H
[11] S. Ohta, T. Kobayashi, T. Asaoka, High lithium ionic conductivity in the garnet-type oxide $Li_{7-X}La_3(Zr_{2-X}, Nb_X)O_{12}$ (x=0-2). J Power Sources 196 (2011) 3342-3345. https://doi.org/10.1016/j.jpowsour.2010.11.089
[12] H. Zhu, J. Liu, Emerging applications of spark plasma sintering in all solid-state lithium-ion batteries and beyond. J Power Sources 391 (2018), 10-25. https://doi.org/10.1016/j.jpowsour.2018.04.054
[13] C.L.Tsai, S. Yu, H. Tempel, H. Kungl, R.A. Eichel, All-ceramic Li batteries based on garnet structured $Li_7La_3Zr_2O_{12}$. Mater Technol (2020) in press. https://doi.org/10.1080/10667857.2020.1746539
[14] L. Cheng, E.J. Crumlin, W. Chen, R. Qiao, H. Hou, S.F. Lux, V. Zorba, R. Russo, R. Kostecki, Z. Liu, K. Persson, W. Yang, J. Cabana, T. Richardson, G. Chen, M. Doeff, The origin of high electrolyte–electrode interfacial resistances in lithium cells containing garnet type solid electrolytes. Phys Chem Chem Phys 16 (2014) 18294-18300. https://doi.org/10.1039/C4CP02921F
[15] G. Larraz, A. Orera, M.L. Sanjuán, Cubic phases of garnet-type Li7La3Zr2O12: the role of hydration. J Mater Chem A 1 (2013) 11419-11428. https://doi.org/10.1039/C3TA11996C
[16] L. Miara, A. Windmüller, C.L. Tsai, W.D. Richards, Q. Ma, S. Uhlenbruck, O. Guillon, G. Ceder, About the compatibility between high voltage spinel cathode materials and solid oxide electrolytes as a function of temperature. ACS Appl Mater Interfaces 8 (2016) 26842-26850. https://doi.org/10.1021/acsami.6b09059
[17] Y. Ren, T. Liu, Y. Shen, Y. Lin, C.W. Nan, Chemical compatibility between garnet-like solid state electrolyte $Li_{6.75}La_3Zr_{1.75}Ta_{0.25}O_{12}$ and major commercial lithium battery cathode materials. J Materiomics 2 (2016) 256-264. https://doi.org/10.1016/j.jmat.2016.04.003
[18] A.M. Laptev, H. Zheng, M. Bram, M. Finsterbusch, O. Guillon, High-pressure field assisted sintering of half-cell for all-solid-state battery. Mater Lett 247 (2019) 155-158. https://doi.org/10.1016/j.matlet.2019.03.109
[19] C.L. Tsai, Q. Ma, C. Dellen, S. Lobe, F. Vondahlen, A. Windmüller, D. Grüner, H. Zheng, S. Uhlenbruck, M. Finsterbusch, F. Tietz, D. Fattakhova-Rohlfing, H.P. Buchkremer, O. Guillon, A garnet structure-based all-solid-state Li battery without interface modification: resolving incompatibility issues on positive electrodes. Sustainable Energy Fuels 3 (2019) 280-291. https://doi.org/10.1039/C8SE00436F
[20] R. Pfenninger, M. Struzik, I. Garbayo, E. Stilp, J.L.M. Rupp, A low ride on processing temperature for fast lithium conduction in garnet solid-state battery films. Nat Energy 4 (2019) 475-483. https://doi.org/10.1038/s41560-019-0384-4
[21] S.P. Woo, W. Lee, Y.S Yoon, Composite cathode material using spark plasma sintering for bulk-type hybrid solid-state batteries. J Korean Phys Soc 73 (2018) 1019-1024. https://doi.org/10.3938/jkps.73.1019

[22] C.L. Tsai, E. Dashjav, E.M Hammer, M. Finsterbusch, F. Tietz, S. Uhlenbruck, H.P. Buchkremer, High conductivity of mixed phase Al-substituted $Li_7La_3Zr_2O_{12}$. J Electroceram 35 (2015) 25-32. https://doi.org/10.1007/s10832-015-9988-7
[23] F. Han, J. Yue, C. Chen, N. Zhao, X. Fan, Z. Ma, T. Gao, F. Wang, X. Guo, C. Wang, Interphase engineering enabled all-ceramic lithium battery. Joule 2 (2018) 497-508. https://doi.org/10.1016/j.joule.2018.02.007
[24] J. Van den Broek, S. Afyon, J.L.M. Rupp, Interface-engineered all-solid-state Li-ion batteries based on garnet-type fast Li^+ conductors. Adv Energy Mater 6 (2016) 1600736. https://doi.org/10.1002/aenm.201600736
[25] C. Shao, Z. Yu, H. Liu, Z. Zheng, N. Sun, C. Diao, Enhanced ionic conductivity of titanium doped $Li_7La_3Zr_2O_{12}$ solid electrolyte. Electrochim Acta 225 (2017) 345-349. https://doi.org/10.1016/j.electacta.2016.12.140
[26] M. Finsterbusch, T. Danner, C.L. Tsai, S. Uhlenbruck, A. Latz, O. Guillon, High capacity garnet-based all-solid-state lithium batteries: fabrication and 3D-microstructure resoled modeling. ACS Appl Mater Interfaces 10 (2018) 22329-22339. https://doi.org/10.1021/acsami.8b06705
[27] J. Wakasugi, H. Munakata, K. Kanamura, Thermal stability of various cathode materials against $Li_{6.25}Al_{0.25}La_3Zr_2O_{12}$ electrolyte. Electrochem 85 (2017) 77-81. https://doi.org/10.5796/electrochemistry.85.77
[28] K. Park, B.C. Yu, J.W. Jung, Y. Li, W. Zhou, H. Gao, S.Son, J.B Goodenough, Electrochemical nature of the cathode interface for a solid-state lithium-ion battery: interface between $LiCoO_2$ and garnet-$Li_7La_3Zr_2O_{12}$. Chem Mater28 (2016) 8051-8059. https://doi.org/10.1021/acs.chemmater.6b03870
[29] M. Bram, A.M. Laptev, T.P. Mishra, K. Nur, M. Kindelmann, M. Ihrig, J.G. Pereira da Silva, R. Steinert, H.P. Buchkremer, A. Litnovsky, F. Klein, J. Gonzalez-Julian, O. Guillon, Application of electric current-assisted sintering techniques for the processing of advanced materials. Adv Eng Mater 22 **(**2020) 2000051. https://doi.org/10.1002/adem.202000051
[30] T. Kato, T. Hamanaka, K. Yamamoto, T. Hirayama, F. Sagane, M. Motoyama, Y. Iriyama, In-situ $Li_7La_3Zr_2O_{12}$/$LiCoO_2$ interface modification for advanced all-solid-state battery. J Power Sources 260 (2014) 292-298. https://doi.org/10.1016/j.jpowsour.2014.02.102
[31] K. Tadanaga, R. Takano, T. Ichinose, S. Mori; A. Hayashi, M. Tatsumisago, Low temperature synthesis of highly ion conductive $Li_7La_3Zr_2O_{12}$–Li_3BO_3 composites. Electrochem Commun 33 (2013) 51-54. https://doi.org/10.1016/j.elecom.2013.04.004
[32] O. Guillon, J. Gonzalez-Julian, B. Dargatz, T. Kessel, G. Schierning, J. Räthel, M. Herrmann, Field-Assisted Sintering Technology/Spark Plasma Sintering: Mechanisms, materials, and technology developments. Adv Eng Mater 16 (2014**)** 830-849. https://doi.org/10.1002/adem.201300409
[33] J. Langer, M.J. Hoffmann, O. Guillon, Electric field-assisted sintering in comparison with the hot pressing of yttria-stabilized zirconia. J Am Ceram Soc 94 (2011) 24-31. https://doi.org/10.1111/j.1551-2916.2010.04016.x
[34] R. Kali, A. Mukhopadhyay, Spark plasma sintered/synthesized dense and nanostructured materials for solid-state Li-ion batteries: Overview and perspective. J Power Sources 247 (2014) 920-931. https://doi.org/10.1016/j.jpowsour.2013.09.010
[35] J.E. Garay, Current-activated, pressure-assisted densification of materials. Annu Rev Mater Res 40 (2010**)** 445-468. https://doi.org/10.1146/annurev-matsci-070909-104433
[36] Y. Zhang, F. Chen, R. Tu, Q. Shen, L. Zhang, Field assisted sintering of dense Al-substituted cubic phase $Li_7La_3Zr_2O_{12}$ solid electrolytes. J Power Sources 268 (2014) 960-964. https://doi.org/10.1016/j.jpowsour.2014.03.148
[37] S.P.Kammampata, R.H. Basappa, T. Ito, H. Yamada, V. Thangadurai, Microstructural and electrochemical properties of alkaline earth metal-doped Li garnet-type solid electrolytes prepared by

solid-state sintering and spark plasma sintering methods. ACS Appl Energy Mater 2 (2019) 1765-1773. https://doi.org/10.1021/acsaem.8b01899
[38] X. Wei, J. Rechtin, E. Olevsky, The fabrication of all-solid-state lithium-ion batteries via spark plasma sintering. Metals 7 2017 372. https://doi.org/10.3390/met7090372
[39] H. El-Shinawi, E.J. Cussen, S.A. Corr, Enhancement of the lithium ion conductivity of Ta-doped $Li_7La_3Zr_2O_{12}$ by incorporation of calcium. Dalton Trans 46 (2017) 9415-9419. https://doi.org/10.1039/C7DT01573A
[40] R. Inada, K. Kusakabe, T. Tanaka, S. Kudo, Y. Sakurai, Synthesis and properties of Al-free $Li_{7-x}La_3Zr_{2-x}TaxO_{12}$ garnet related oxides. Solid State Ion 262 (2014) 568-572. https://doi.org/10.1016/j.ssi.2013.09.008
[41] H. Takahara, T. Takeuchi, M. Tabuchi, H. Kageyama, Y. Kobayashi, Y. Kurisu, S. Kondo, R. Kanno, All-solid-state lithium secondary battery using oxysulfide glass: addition and coating of carbon to positive electrode. J Electrochem Soc 151 (2004) A1539-A1544. 10.1149/1.1784172
[42] E. Antolini, M. Ferretti, Synthesis and thermal stability of $LiCoO_2$. J Solid State Chem 117 (1995) 1-7. https://doi.org/10.1006/jssc.1995.1238
[43] K.H. Kim, Y. Iriyama, K. Yamamoto, S. Kumazaki, T. Asaka, K. Tanabe, C.A.J. Fisher, T. Hirayama, R. Murugan, Z. Ogumi, Characterization of the interface between $LiCoO_2$ and $Li_7La_3Zr_2O_{12}$ in an all-solid-state rechargeable lithium battery. J Power Sources 196 (2011) 764-767. https://doi.org/10.1016/j.jpowsour.2010.07.073
[44] S. Uhlenbruck, J. Dornseiffer, S. Lobe, C. Dellen, C.L. Tsai, B. Gotzen, D. Sebold, M. Finsterbusch, O. Guillon, Cathode-electrolyte material interactions during manufacturing of inorganic solid-state lithium batteries. Journal Electroceram 38 (2017) 197-206. https://doi.org/10.1007/s10832-016-0062-x
[45] H. Yamada, T. Ito, R.H. Basappa, Sintering mechanisms of high-performance garnet-type solid electrolyte densified by spark plasma sintering. Electrochim Acta 222 (2016), 648-656. https://doi.org/10.1016/j.electacta.2016.11.020
[46] C. Deviannapoorani, L. Dhivya, S. Ramakumar, R. Murugan, Lithium ion transport properties of high conductive tellurium substituted $Li_7La_3Zr_2O_{12}$ cubic lithium garnets. J Power Sources 240 (2013) 18-25. https://doi.org/10.1016/j.jpowsour.2013.03.166
[47] K.H. Kim, Y. Iriyama, K. Yamamoto, S. Kumazaki, T. Asaka, K. Tanabe, C. Fisher, T. Hirayama, R. Murugan, Z .Ogumi, Characterization of the interface between $LiCoO_2$ and $Li_7La_3Zr_2O_{12}$ in an all-solid-state rechargeable lithium battery. 196 (2011) 764–767. https://doi.org/10.1016/j.jpowsour.2010.07.073
[48] A. Sharafi, S. Yu, M. Naguib, M. Lee, C. Ma, H.M. Meyer, J. Nanda, M. Chi, D.J. Siegel, J. Sakamoto, Impact of air exposure and surface chemistry on Li–$Li_7La_3Zr_2O_{12}$ interfacial resistance. J Mater Chem A 5 (2017) 13475-13487.
[49] W. Xia, B. Xu, H. Duan, Y. Guo, H. Kang, H. Li, H. Liu, Ionic conductivity and air stability of Al-doped $Li_7La_3Zr_2O_{12}$ sintered in alumina and Pt crucibles. ACS Appl Mater Interface 8 (2016) 5335-5342. https://doi.org/10.1021/acsami.5b12186
[50] W. Xia, B. Xu, H. Duan, X. Tang, Y. Guo, H. Kang, H. Li, H. Liu, , Reaction mechanisms of lithium garnet pellets in ambient air: The effect of humidity and CO_2. J Am Ceram Soc 100 (2017**)** 2832-2839. https://doi.org/10.1111/jace.14865
[51] Y. Wang, W. Lai, Phase transition in lithium garnet oxide ionic conductors $Li_7La_3Zr_2O_{12}$: The role of Ta substitution and H_2O/CO_2 exposure. J Power Sources 275 (2015) 612-620. https://doi.org/10.1016/j.jpowsour.2014.11.062
[52] Y. Li, X. Chen, A. Dolocan, Z. Cui, S. Xin, L. Xue, H. Xu, K. Park, J.B. Goodenough, Garnet electrolyte with an ultralow interfacial resistance for Li-metal batteries. J Am Chem Soc 140 (2018) 6448-6455. https://doi.org/10.1021/jacs.8b03106

[53] J. Guo, H. Guo, A.L. Baker, M.T. Lanagan, E.R. Kupp, G.L. Messing, C.A. Randall, Cold sintering: A paradigm shift for processing and integration of ceramics. Angew Chem Int Ed 55 (2016) 11457-11461. https://doi.org/10.1002/anie.201605443
[54] H. Leng, J. Huang, J. Nie, J. Luo, Cold sintering and ionic conductivities of $Na_{3.256}Mg_{0.128}Zr_{1.872}Si_2PO_{12}$ solid electrolytes. J Power Sources 391 (2018) 170-179. https://doi.org/10.1016/j.jpowsour.2018.04.067
[55] R. Koerver, W. Zhang, L. De Biasi, S. Schweidler, A.O. Kondrakov, S. Kolling, T. Brezesinski, P. Hartmann, W.G. Zeier, J. Janek, Chemo-mechanical expansion of lithium electrode materials – on the route to mechanically optimized all-solid-state batteries. Energy Environ Sci 11 (2018) 2142-2158. https://doi.org/10.1039/C8EE00907D
[56] M. Duffiet, M. Blangero, P.E. Cabelguen, C. Delmas, D. Carlier, Influence of the initial Li/Co ratio in $LiCoO_2$ on the high-voltage phase-transitions mechanisms. J Phys Chem Lett 9 (2018) 5334-5338. https://doi.org/10.1021/acs.jpclett.8b02252
[57] F. Han, Y. Zhu, X. He, Y. Mo, C. Wang, Electrochemical stability of $Li_{10}GeP_2S_{12}$ and $Li_7La3Zr_2O_{12}$ solid electrolytes. Adv Energy Mater 6 (2016) 1501590. https://doi.org/10.1002/aenm.201501590